PCCP

ROYAL SOCIETY OF CHEMISTRY

PAPER

View Article Online
View Journal | View Issue

Cite this: *Phys. Chem. Chem. Phys.*, 2022, **24**, 28465

Group theory analysis of phonons in monolayer chromium trihalides and their Janus structures

Y. C. Liu, *[a] H. B. Niu, [b] J. B. Lin [c] and V. Wang *[a]

A contrastive investigation of the symmetry aspects of phonons in monolayer chromium trihalides and their Janus structures Y_3–Cr_2–X_3 (X, Y = F, Cl, Br, I) was presented within group theory. We classified all phonon vibration modes at the Brillouin-zone center (Γ) into irreducible representations. The infrared and Raman activity of optic phonons, Raman tensors, and the possible polarization assignments of Raman active phonons are further predicted. We clarify the discrepancy concerning the Raman and infrared activity of optic modes in monolayer CrI_3. It is also found that the Raman and infrared spectra are exclusive for X_3–Cr_2–X_3 but coincident for Janus Y_3–Cr_2–X_3. This distinction plays a vital role in optic spectra identification of the Janus Y_3–Cr_2–X_3 monolayer from the X_3–Cr_2–X_3 monolayer. To demonstrate the origin of phonon chirality and magnetism intuitively, we derive the symmetry-matched phonon eigenfunctions and the corresponding schematic representations of the eigenvectors for both the F_3–Cr_2–I_3 and I_3–Cr_2–I_3 monolayers. Our analysis indicates that the spin–phonon coupling, the magneto-optical effect of infrared and Raman active phonons, and the phonon chirality could be observed in the Janus Y_3–Cr_2–X_3 monolayer more easily than in the X_3–Cr_2–X_3 monolayer. Our results thus provide a detailed guiding map for experimental identification and characterization of the Janus Y_3–Cr_2–X_3 monolayer.

Received 31st July 2022,
Accepted 31st October 2022

DOI: 10.1039/d2cp03510c

rsc.li/pccp

I. Introduction

Since the experimental demonstration of magnetism in a two-dimensional (2D) CrI_3 monolayer,[1,2] its stacking, strain and electric-field tunable anisotropic magnetism have been extensively and deeply studied in recent years.[3–8] Recently, various phonon-related effects in single- and multi-layer CrI_3 have also been explored theoretically and experimentally.[9–13]

Larson and Kaxiras obtained the frequencies and irreducible representations of the optic phonon at the Brillouin-zone center (Γ) in bulk and monolayer CrI_3 by an *ab initio* study,[14] while Webster *et al.* investigated the spin–lattice and spin–phonon interactions in monolayer magnetic CrI_3 and obtained the phonon band dispersion as well as the schematic representation of the eigenvectors for all phonon vibrational modes at the Γ point.[15] Some discrepancies, however, still exist in the literature[16,17] in regard to the symmetry classification of crystal vibrational modes, the identification of Raman (R), and the infrared (IR) activity of optic phonons in the CrI_3 monolayer. Thus a systematic group theory analysis of phonons in monolayer CrX_3 with (X = F, Cl, Br, I) is still necessary to clarify these issues.

Meanwhile, the excellent electronic and piezoelectric properties observed in the Janus monolayer of transition metal dichalcogenides (TMDs)[18–22] motivate researchers to synthesize more novel Janus candidates.[23,24] The magnetic CrI_3 monolayer is a typical example of this. Although the electronic structure and magnetic anisotropy of Janus CrX_3 monolayers have been investigated recently,[25–27] our latest work still reveals a large vertical electric polarization of up to -0.155×10^{-10} C m^{-1} in the Janus CrX_3 monolayer due to the absence of inversion symmetry.[28] However, as far as we know, a systematical group theory analysis of phonons in the Janus CrX_3 monolayer is still absent in the literature.

In addition, the theoretical prediction of chiral phonons[29] and its experimental verification in tungsten-diselenide monolayers[30] inspire many researchers to explore chiral phonons in other 2D as well as three-dimensional (3D) materials.[31–37] For example, Yin *et al.* showed that a magnetic $CrBr_3$ monolayer hosts chiral phonons at the Brillouin-zone center.[38] These chiral phonons are special linear combinations of the doubly-degenerate E_g phonons, whose eigenvectors exhibit clockwise and counterclockwise rotations with angular momentum, and can completely switch the polarization of incident circularly polarized light. Subsequently, a question naturally arises: can chiral phonons be observed in Janus CrX_3 with (X = F, Cl, Br, I) monolayer, and what are the unique properties that distinguish them from the inversion-symmetric CrX_3 monolayer?

In this study, we attempt to answer these questions by performing a comprehensive and systematic group theory

[a] *Department of Applied Physics, Xi'an University of Technology, Xi'an 710054, China. E-mail: liuyachao@xaut.edu.cn, wangvei@icloud.com*
[b] *Department of Applied Physics, Xi'an Jiaotong University City College, Xi'an 710018, China*
[c] *National Institute for Materials Science, Tsukuba, 305-0044, Japan*

analysis of phonons in chromium trihalides monolayers and their Janus structures denoted by an intuitive form Y_3–Cr_2–X_3 with (X, Y) ∈ (F, Cl, Br, I). The irreducible representations and eigenvectors of phonons at the Γ point for inversion-asymmetric Janus Y_3–Cr_2–X_3 and inversion-symmetric X_3–Cr_2–X_3 monolayers are deduced first. Then the IR and R activity of phonons, as well as Raman tensors of the polarization setup of R active phonons, are presented. Besides, the compatibility relationship of phonon irreducible representations between the Y_3–Cr_2–X_3 and X_3–Cr_2–X_3 monolayer is also offered. At last, we discuss the spin–phonon coupling and the magneto-optical effect of IR and R active phonons as the chiral phonons in the Y_3–Cr_2–X_3 and X_3–Cr_2–X_3 monolayer. Our work clarifies the R activity of optic phonons in CrI_3 monolayer and offers systematic information about phonons in Janus Y_3–Cr_2–X_3 monolayers. Our results are expected to be a guide to identifying and characterizing the optical spectra of the Janus Y_3–Cr_2–X_3 monolayer.

II. Symmetry analysis of the Y_3–Cr_2–X_3 monolayer

A. Real space symmetry and wave vector group at the Brillouin zone center

Laser Raman scattering and infrared absorption spectra are both powerful tools for the structural identification and characterization of 3D materials. Since they have been successfully applied to 2D graphene, transition metal dichalcogenides, and phosphorene,[39–41] they have also been the standard optical techniques to characterize the properties of 2D materials. The group theory classification of phonons in 2D materials can provide the irreducible representations of all phonons at the Γ point as well as their IR and R activities which are essential pieces of information for the polarization setup of the incident (scattering) light and the identification of optical spectra in infrared and Raman spectroscopy.

We begin by deriving the symmetry classification of phonon modes at the Γ point and then point out the IR and R activity of the optic modes in the Janus Y_3–Cr_2–X_3 monolayer. The unit cell of the Y_3–Cr_2–X_3 monolayer consists of three Y and three X atoms as well as two Cr atoms, in total eight atoms. Thus there are 24 phonon branches, including 3 acoustic and 21 optic branches. The F_3–Cr_2–I_3 monolayer, whose crystal structure is shown in Fig. 1, can be taken as an example. We have demonstrated its dynamic stability since there is no imaginary frequency in the phonon dispersion of the Janus F_3–Cr_2–I_3 monolayer.[28] Generally, lattice vibrational modes can be classified based on the irreducible representation of the space group.[42] The structural symmetry of the Janus Y_3–Cr_2–X_3 monolayer belongs to the symmorphic space group No. 157. It has the symmetry designation C_{3v}^2 in accord with the Schoenflies notation, and $P31m$ in the Hermann–Mauguin notation.

The rotational aspects for real space and the group of the wave vector at $k = 0$ in reciprocal space (Γ point) are described by the point group C_{3v}. Its character table is given in Table 1, where Γ_i (i = 1, 2, 3) are Bethe symbols of the space group for

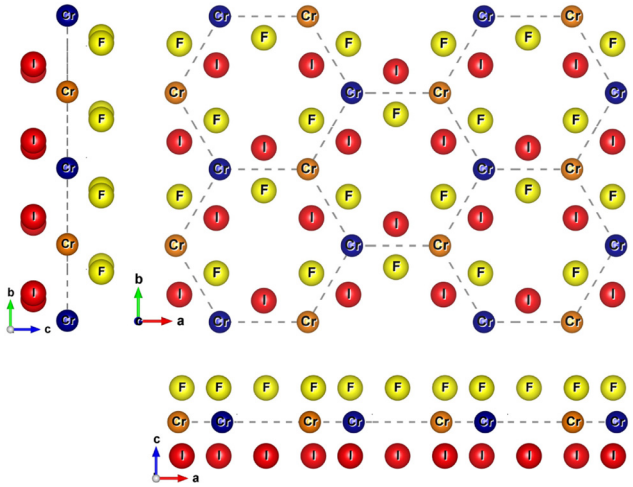

Fig. 1 The lattice structure of monolayer F_3–Cr_2–I_3, where orange and blue spheres with the same size represent Cr atoms on different sites, while yellow and red spheres with different sizes represent F and I atoms, respectively, as indicated on each atom. This color convention applies to all subsequent phonon oscillations figures.

irreducible representation at the Γ point, and A and E are Mulliken signs of the point group of one-dimensional (1D) and 2D irreducible representations; the subscripts 1 and 2 denote representations that are symmetric and antisymmetric to the mirror reflection operation σ_v; x, y, z and R_x, R_y, R_z are basis components of polar and axial vectors, respectively. Table 1 shows that C_{3v} has only three irreducible representations.

B. Irreducible representations for vibrational modes in the Y_3–Cr_2–X_3 monolayer

The lattice vibrational modes of Y_3–Cr_2–X_3 at Γ are classified according to the irreducible representations of C_{3v}. Characters of atomic displacement vector representations, primitive cell equivalent representations, and lattice vibration representations of Y_3–Cr_2–X_3 are listed in Table 2. These representations can be reduced to the irreducible representations summarized in Table 1:

$$\Gamma_{\text{vector}} = \text{A}_1 \oplus \text{E}, \tag{1}$$

$$\Gamma_{\text{equivalent}} = 3\text{A}_1 \oplus \text{A}_2 \oplus 2\text{E}, \tag{2}$$

$$\begin{aligned}\Gamma_{\text{vibration}} &= \Gamma_{\text{vector}} \otimes \Gamma_{\text{equivalent}} \\ &= (\text{A}_1 \oplus \text{E}) \otimes (3\text{A}_1 \oplus \text{A}_2 \oplus 2\text{E}) \\ &= 5\text{A}_1 \oplus 3\text{A}_2 \oplus 8\text{E},\end{aligned} \tag{3}$$

$$\begin{aligned}\Gamma^z_{\text{vibration}} &= \text{A}_1 \otimes (3\text{A}_1 \oplus \text{A}_2 \oplus 2\text{E}) \\ &= 3\text{A}_1 \oplus \text{A}_2 \oplus 2\text{E},\end{aligned} \tag{4}$$

Table 1 Character table for the point group C_{3v} including basis functions of the irreducible representations[42]

SG	PG	E	$2C_3$	$3\sigma_v$	Basis functions
Γ_1	A_1	1	1	1	z, z^2, $x^2 + y^2$
Γ_2	A_2	1	1	−1	R_z
Γ_3	E	2	−1	0	(x, y), (R_x, R_y), (xz, yz), (x^2-y^2, xy)

Table 2 Characters of vector, equivalent, and vibration representations for Y_3–Cr_2–X_3 in the C_{3v}^2 crystal structure as well as characters for X, Y, and Cr atoms on different Wyckoff sites denoted by 2b and 3c

C_{3v}	E	C_3	σ_v
χ_{vector}	3	0	1
$\chi_{equivalent}$	8	2	2
$\chi_{vibration}$	24	0	2
$\chi_X(3c)$	3	0	1
$\chi_Y(3c)$	3	0	1
$\chi_{Cr}(2b)$	2	2	0

$$\begin{aligned}\Gamma_{\text{vibration}}^{(x,y)} &= E \otimes (3A_1 \oplus A_2 \oplus 2E) \\ &= 2A_1 \oplus 2A_2 \oplus 6E,\end{aligned} \tag{5}$$

where Γ_{vector}, $\Gamma_{\text{equivalent}}$, and $\Gamma_{\text{vibration}}$ are the symmetry representations of the atomic displacement vector, the equivalent representations of the primitive cell and the symmetry representations of lattice vibration at the Γ point, respectively. The equivalent representation denotes the number of atoms that are invariant under the symmetry operations of the group. The symmetry representation of lattice vibration is equal to the direct product of the symmetry representations of the atomic displacement vector and the equivalent representations of the primitive cell.[42,43] We show that lattice vibration at the zone center in monolayer Y_3–Cr_2–X_3 includes 24 phonon modes, in which there are 8 non-degenerate modes ($5A_1 + 3A_2$) and 8 doubly degenerate E modes. Note that the vector transforming as $A_1 \oplus E$ corresponds to z and (x, y) components, and it permits us to separate the lattice modes vibrating along the z-direction from those in the x–y plane. The irreducible representations for out-of-plane and in-plane modes are described through eqn (4) and (5), respectively.

III. Irreducible representations for optic modes in the Y_3–Cr_2–X_3 monolayer

The symmetry representation of 24 phonon modes can be further decomposed into the representations of acoustic and optic modes as follows:

$$\Gamma_{\text{acoustic}} = A_1 \oplus E, \tag{6}$$

$$\begin{aligned}\Gamma_{\text{optic}} &= \Gamma_{\text{vibration}} - \Gamma_{\text{acoustic}} \\ &= \{4A_1 \oplus 7E\}(\text{IR} + \text{R}) \oplus 3A_2(\text{silent}),\end{aligned} \tag{7}$$

$$\begin{aligned}\Gamma_{\text{optic}}^{z} &= 2A_1 \oplus A_2 \oplus 2E \\ &= \{2[A_1 \oplus E]\}(X + Y) \oplus A_2(Cr),\end{aligned} \tag{8}$$

$$\begin{aligned}\Gamma_{\text{optic}}^{(x,y)} &= 2A_1 \oplus 2A_2 \oplus 5E \\ &= \{2[A_1 \oplus E] \oplus 2[A_2 \oplus E]\}(X + Y) \oplus E(Cr).\end{aligned} \tag{9}$$

The acoustic modes transform as a polar vector and thus include one A_1 and one E mode. The frequency of the three acoustic modes at Γ is identical to zero. In contrast, the rest of the 21 nonzero-frequency modes belong to optic modes, which include four A_1 and three A_2 non-degenerate modes as well as seven doubly degenerate E modes. For Cr atoms there is one out-of-plane (z) A_2 mode and one in-plane (x–y) E mode; for six halogen atoms (3X + 3Y), there are two pairs of $A_1 \oplus E$ out-of-plane modes as well as four pairs of $A_{1(2)} \oplus E$ in-plane modes.

A. IR and R activity of optic modes in the Y_3–Cr_2–X_3 monolayer

IR active modes are symmetry-adapted modes that transform according to the vector representation, while the R active modes are symmetry-adapted modes that transform according to the components of a symmetric second-rank tensor representation corresponding to quadratic basis functions. From the basis functions shown in Table 1 one can determine that the eighteen optic modes $\{4A_1 \oplus 7E\}$ are both R and IR active. The remaining three A_2 optic modes are neither R nor IR active, which cannot be detected by first-order Raman and infrared optical spectra and are thus called silent modes. However, all three silent A_2 modes can be detected in the second-order Raman spectrum since the overtone of A_2 modes becomes an R active mode A_1 ($A_2 \otimes A_2 = A_1$). In fact, for Janus X_3–Cr_2–Y_3, all the fundamental optic modes at the Γ point are second-order R active modes.

According to eqn (8), there are six out-of-plane optic modes, including two A_1 and two degenerate E, which are both infrared and Raman active, and may correspond to four Raman peaks. Eqn (9) shows that there are nine in-plane modes. Seven of these modes are expected to be both infrared and Raman active with two A_1 and five E peaks in the spectra. It is worth pointing out that the above symmetry analysis is suitable for all Janus phases of Y_3–Cr_2–X_3, with X and Y belonging to halogen elements, *i.e.*, (F, Cl, Br, I) but without X = Y. In addition, all R active (also IR active) modes become extraordinary phonons since the Y_3–Cr_2–X_3 monolayer is a mono-axis polar material with an optic axis along the out-of-plane direction. It is well-known that when the wave vector is parallel or perpendicular to the optic axis, the extraordinary phonons become transverse modes (in this case A_{1T} and E_T) and its electric polarization becomes zero. Therefore, the electric polarity of Y_3–Cr_2–X_3 does not affect the direction dispersion of the optic phonons.

B. Optic modes in monolayer X_3–Cr_2–X_3

In sharp contrast to the coexistence of R and IR activity in Janus Y_3–Cr_2–X_3, in the X_3–Cr_2–X_3 the R and IR active modes are mutually exclusive due to the intrinsic inversion symmetry. To identify the X_3–Cr_2–Y_3 structure from a Raman optical spectrum experiment, we compare the R active modes of Janus Y_3–Cr_2–X_3 with CrX_3 (X_3–Cr_2–X_3) possessing inversion symmetry. The space group of X_3–Cr_2–X_3 is D_{3d}^1 ($P\bar{3}1m$, No. 162), whose factor group is D_{3d}.[14,44] The character table for D_{3d} is given in Table 3, where the subscripts g (gerade) and u (ungerade) denote representations that are symmetric and antisymmetric concerning the inversion operation; the other symbols are the same as that in Table 1. It is noted that point group D_{3d} has six irreducible representations which is twice as many as that of

Table 3 Character table for the point group D_{3d} including basis functions of the irreducible representations[42]

SG	PG	E	$2C_3$	$3C_2$	i	$2S_6$	$3\sigma_d$	Basis functions
Γ_1^+	A_{1g}	1	1	1	1	1	1	z^2, x^2+y^2
Γ_2^+	A_{2g}	1	1	−1	1	1	−1	R_z
Γ_3^+	E_g	2	−1	0	2	−1	0	(R_x, R_y), (x^2-y^2, xy), (xz, yz)
Γ_1^-	A_{1u}	1	1	1	−1	−1	−1	
Γ_2^-	A_{2u}	1	1	−1	−1	−1	1	z
Γ_3^-	E_u	2	−1	0	−2	1	0	(x,y)

C_{3v}. Three of them are inversion symmetric and the remaining three are inversion antisymmetric.

We classify the lattice vibrational modes of X_3–Cr_2–X_3 at Γ by group theory based on the irreducible representations of D_{3d}. Taking I_3–Cr_2–I_3 as an example, we list its characters of atomic displacement vector representations, primitive cell equivalent representations, and lattice vibration representations in Table 4. These representations can be decomposed into the irreducible representations summarized in Table 3:

$$\Gamma_{\text{vector}} = A_{2u} \oplus E_u, \tag{10}$$

$$\Gamma_{\text{equivalent}} = 2A_{1g} \oplus A_{1u} \oplus A_{2u} \oplus E_g \oplus E_u, \tag{11}$$

$$\begin{aligned}\Gamma_{\text{vibration}} &= \Gamma_{\text{vector}} \otimes \Gamma_{\text{equivalent}} \\ &= (A_{2u} \oplus E_u) \otimes (2A_{1g} \oplus A_{1u} \oplus A_{2u} \oplus E_g \oplus E_u) \\ &= 2A_{1g} \oplus 2A_{2g} \oplus A_{1u} \oplus 3A_{2u} \oplus 4E_g \oplus 4E_u,\end{aligned} \tag{12}$$

$$\Gamma_I = A_{1g} \oplus A_{2u} \oplus E_g \oplus E_u, \tag{13}$$

$$\Gamma_{Cr} = A_{1g} \oplus A_{1u}. \tag{14}$$

This symmetry representation of lattice vibration still includes 24 phonon modes and can also be decomposed into the representations of acoustic and optic modes as follows:

$$\Gamma_{\text{acoustic}} = A_{2u} \oplus E_u, \tag{15}$$

$$\Gamma_{\text{optic}} = (2A_{1g} \oplus 4E_g) \oplus 2A_{2g} \oplus A_{1u} \oplus [2A_{2u} \oplus 3E_u], \tag{16}$$

$$\Gamma_{Cr}^{z} = (A_{1g} \oplus A_{1u}) \otimes A_{2u} = A_{2u} \oplus A_{2g}, \tag{17}$$

$$\Gamma_{Cr}^{(x,y)} = (A_{1g} \oplus A_{1u}) \otimes E_u = E_u \oplus E_g, \tag{18}$$

$$\begin{aligned}\Gamma_I^{z} &= (A_{1g} \oplus A_{2u} \oplus E_g \oplus E_u) \otimes A_{2u} \\ &= A_{2u} \oplus A_{1g} \oplus E_u \oplus E_g,\end{aligned} \tag{19}$$

$$\begin{aligned}\Gamma_I^{(x,y)} &= (A_{1g} \oplus A_{2u} \oplus E_g \oplus E_u) \otimes E_u \\ &= A_{1g} \oplus A_{2g} \oplus A_{1u} \oplus A_{2u} \oplus 2E_g \oplus 2E_u.\end{aligned} \tag{20}$$

Table 4 Characters of vector, equivalent, and vibration representations for I_3–Cr_2–I_3 as well as characters for I and Cr atoms on different Wyckoff sites denoted by 6k and 2c

D_{3d}	E	$2C_3$	$3C_2$	i	$2S_6$	$3\sigma_d$
χ_{vector}	3	0	−1	−3	0	1
$\chi_{\text{equivalent}}$	8	2	2	0	0	2
$\chi_{\text{vibration}}$	24	0	−2	0	0	2
χ_I(6k)	6	0	0	0	0	2
χ_{Cr}(2c)	2	2	2	0	0	0

We point out that $(2A_{1g} \oplus 4E_g)$ are 10 Raman active modes, while $[2A_{2u} \oplus 3E_u]$ are 8 IR active modes. Our results about the irreducible representation of the fundamental optic modes in X_3–Cr_2–X_3 are in good agreement with that of the CrI_3 monolayer obtained by Larson *et al.*[14] The R and IR modes in X_3–Cr_2–X_3 are exclusive due to the presence of inversion symmetry in point group D_{3d}. Note that this exclusion principle does not always mean that all the g modes are Raman active and the u modes are IR active. The remaining 3 optic modes, $2A_{2g} \oplus A_{1u}$, are silent modes.

The reason why we derived in detail the symmetry classification of phonons in the CrI_3 monolayer here is the discrepancies existing in the literature and the positive citations of a false result. We find that the two silent A_{2g} phonons of CrI_3 have been misidentified as R active modes,[15] while the silent A_{1u} phonon of the CrI_3 monolayer has been misidentified as the IR active mode.[16] Besides, based on our results, we find that the acoustic A_{2u} has been misjudged as A_{1u} in Webster *et al.*'s results,[15] and therefore the wrong number of the two modes in $\Gamma_{D_{3d}}$. The last but most important point, is that they also made the misidentification of irreducible representations for modes (j) 134.5 cm^{-1} (A_{2u}) and (n) 264.7 cm^{-1} (A_{1u}) in Fig. 4,[15] the correct result should be A_{1u} for the (j) mode and A_{2u} for the (n) mode. Since this misidentification has misled the experimental identification of IR active modes of the CrI_3 monolayer,[16,17] we commented on Webster *et al.*'s results[45] and they have since made a correction.[46] We hope that our detailed derivation will help further correct other relevant errors in the literature.

In addition, the out-of-plane and in-plane modes of chromium and halogen atoms are found to be easily distinguishable. Specifically, both of the A_{1g} Raman active modes originate merely from the optic vibration of halogen atoms, while Cr atoms only take part in the Raman active E_g modes. Considering that the magnetism of CrI_3 comes from Cr atoms,[1,2,47] the spin-Raman phonon coupling should be significant in the E_g modes involving vibration of Cr atoms. This has been verified in the linear polarized Raman spectra for monolayer CrI_3.[14,15]

C. Compatibility relationship between monolayer Y_3–Cr_2–X_3 and X_3–Cr_2–X_3

The compatibility relationship for group-subgroup pairs from D_{3d} to C_{3v} is shown in Table 5. Note that inversion symmetry disappears when the symmetry is degraded from D_{3d} to C_{3v}. This makes the g and u subscripts also disappear in the notation of irreducible representation of C_{3v}. The compatibility relationship is not trivial since that the A_{1u} becomes A_2, while A_{2u} turns into A_1. This is due to the subscript 1 and 2 in D_{3d} and C_{3v} with different meanings for one-dimensional irreducible representations. From Tables 1 and 3, one can determine that the subscript 1(2) of the irreducible representation in C_{3v} denotes symmetric (anti-symmetric) relative to mirror σ, while in D_{3d} it denotes symmetric (anti-symmetric) relative to rotation

Table 5 Correlation table for D_{3d} and C_{3v} point groups

D_{3d}		C_{3v}	
Γ_1^+	A_{1g}	Γ_1	A_1
Γ_2^+	A_{2g}	Γ_2	A_2
Γ_3^+	E_g	Γ_3	E
Γ_1^-	A_{1u}	Γ_2	A_2
Γ_2^-	A_{2u}	Γ_1	A_1
Γ_3^-	E_u	Γ_3	E

C_2. For the inversion symmetric representation in D_{3d}, subscripts 1 and 2 are of the same meaning as to mirror σ_d; for inversion antisymmetric representation, they are of the inverse meaning as to mirror σ_d.

Using this transformation as shown in Table 5, one can obtain the irreducible representations of vibrational modes of Y_3–Cr_2–X_3 with C_{3v} symmetry from that of X_3–Cr_2–X_3 with D_{3d} symmetry directly. It is found that the Raman modes A_{1g} and E_g in D_{3d} transform to A_1 and E in C_{3v}; comparatively, the IR modes A_{2u} and E_u in D_{3d} also transform to A_1 and E. However, A_1 and E are both R and IR active modes in C_{3v}. Therefore, we conclude that the Raman and infrared spectra are mutually exclusive for X_3–Cr_2–X_3, but they are coincident for Janus Y_3–Cr_2–X_3. This distinct difference can be used to identify the Janus structure from its mother high-symmetry structure. In addition, the three silent modes $2A_{2g} \oplus A_{1u}$ in X_3–Cr_2–X_3 are all transformed to A_2 modes in Y_3–Cr_2–X_3, which still remain silent.

D. Raman tensor of optic modes in monolayer Y_3–Cr_2–X_3 and X_3–Cr_2–X_3

The use of linear polarized light plays a major role in the assignment of experimentally observed Raman peaks to specific R modes. In Raman experiments with linear polarized light, Porto's notation $\mathbf{k}_i(\mathbf{e}_i\mathbf{e}_s)\mathbf{k}_s$ is generally used to denote the incident propagation direction $\mathbf{k}_i$, the incident and scattered polarization directions $(\mathbf{e}_i\mathbf{e}_s)$ and the scattered propagation direction $\mathbf{k}_s$, where $\mathbf{e}_i$ and $\mathbf{e}_s$ are the incident and the scattered electric fields, respectively. The scattered light is traditionally designated as having diagonal Raman components $(\mathbf{e}_i \| \mathbf{e}_s)$, or off-diagonal Raman components $(\mathbf{e}_i \perp \mathbf{e}_s)$.

Table 6 shows the symmetric form of the Raman polarizability tensor and the possible polarization assignments of the incident and the scattered electric field for observing the Raman active modes with C_{3v} and D_{3d} point group structures.

For the X_3–Cr_2–X_3 monolayer of D_{3d} point groups, there are two types of R active modes A_{1g} and E_g. Considering both the permitted polarization assignments in Table 6 of the incident and the scattered electric field and eqn (16), we conclude that one can observe six Raman peaks (both $2A_{1g}$ and $4E_g$) in parallel polarization laser set-up and only four E_g in perpendicular (or crossing) polarization laser set-ups. This conclusion agrees well with the other theoretical and experimental polarized Raman spectra for monolayer CrI_3.[14,15,44]

For the Y_3–Cr_2–X_3 monolayer of C_{3v} point groups, there are also two R active modes A_1 and E. Considering both the permitted polarization assignments on the bottom of Table 6 of the incident and the scattered electric field and eqn (16), we conclude that one can observe in principle eleven Raman peaks (both $4A_1$ and 7E) in parallel polarization laser set-up and seven Raman peaks corresponding to E modes in perpendicular polarization laser set-ups. Specifically, if one detects the scattered polarized light in the same polarization direction as the incident polarized light, he or she can observe both A_1 and E modes; in contrast, if one probes the scattered polarized light in the polarization direction perpendicular to that of incident polarized light, then only degenerate E modes can be observed.

Table 6 Irreducible representations of R active modes and Raman tensor for both C_{3v} and D_{3d} point groups

A_1	$E(y)$	$E(-x)$
A_{1g}	E_g	E_g
$\begin{pmatrix} a & 0 & 0 \\ 0 & a & 0 \\ 0 & 0 & b \end{pmatrix}$	$\begin{pmatrix} c & 0 & 0 \\ 0 & -c & d \\ 0 & d & 0 \end{pmatrix}$	$\begin{pmatrix} 0 & -c & -d \\ -c & 0 & 0 \\ -d & 0 & 0 \end{pmatrix}$
$(\mathbf{e}_i \| \mathbf{e}_s)$.	$(\mathbf{e}_i \| \mathbf{e}_s)$ and $(\mathbf{e}_i \perp \mathbf{e}_s)$.	$(\mathbf{e}_i \perp \mathbf{e}_s)$
(e_{ix},e_{sx})	(e_{ix},e_{sx})	(e_{ix},e_{sy})
(e_{iy},e_{sy})	(e_{iy},e_{sy})	(e_{iy},e_{sx})
(e_{iz},e_{sz})	(e_{iy},e_{sz})	(e_{ix},e_{sz})
	(e_{iz},e_{sy})	(e_{iz},e_{sx})

Moreover, we note that for the R active mode with A_1 symmetry in the first column of Table 6, the induced dipole has the same laser polarization direction as the incident electric field, thus it can only be detected by the parallel set-up of polarization. For two-dimensional materials, the incident light and detector are usually installed along the z direction with a back-scattering structure, and the permitted polarization is in the x and y directions. Thus there are twelve in-plane R modes for the Y_3–Cr_2–X_3 monolayer that may be observed by the parallel set-up of polarization, corresponding to seven Raman peaks in spectroscopy: two non-degenerate A_1 peaks and five doubly degenerate E peaks.

IV. Vibrational eigenvectors of optic modes

A. Eigenvectors of optic modes in F_3–Cr_2–I_3

The vibration directions of IR and R active modes are vital for setting the incident and detection directions as well as the polarization of the light used in optical spectra experiments. Therefore, we analyze the vibrational eigenvectors of optic modes in monolayer F_3–Cr_2–I_3, which is also suitable for other Janus Y_3–Cr_2–X_3 monolayers with the same symmetry. First, the out-of-plane optic modes for monolayer F_3–Cr_2–I_3 are depicted in Fig. 1. One can see that the A_2 mode is a z-axis bending mode for two Cr atoms in the unit cell. Both the A_1 modes are stretching modes along the z-direction: one is only for halogen atoms and the other is combined in anti-phase with Cr atoms. One partner of E modes is related to the corresponding A_1

modes by combining the $(1,\omega,\omega^2)$ phases with three fluorine and three iodine atoms, respectively, where ω denotes the phase factor $e^{i2\pi/3}$ related to three-fold rotation operation; the other partner of the E mode is the complex conjugate of the former and is acquired by the interchange of ω and ω^2.

The in-plane optic modes for halogen atoms (three fluorine and three iodine) in monolayer F_3–Cr_2–I_3 are shown in Fig. 3 and 4. Fig. 3 displays the four in-plane tangential modes, including two A_2 and two E modes. We find that the two A_2 are rocking modes with one in-phase and the other antiphase for F and I atoms. The in-phase A_2 mode has a corresponding E mode shown below, which is obtained similarly to that for the z-axis A_1 mode shown in Fig. 2(c).

Fig. 4 shows the four in-plane radial modes, including two A_1 and two E modes. It is found that both the A_1 modes are breathing modes with one in-phase and the other antiphase for F and I atoms. The corresponding E modes shown below are also obtained similarly to that for the in-plane A_2 mode shown in Fig. 3(c). Since the relative phase factors for the three F and I atoms in these E modes are similar to that of three-phase alternating current, we call them 'three-phase' breathing modes. But strictly speaking, the E modes stemming from the A_1 breathing mode are not breathing modes because the corresponding vibrations change the symmetry of the unit cell.

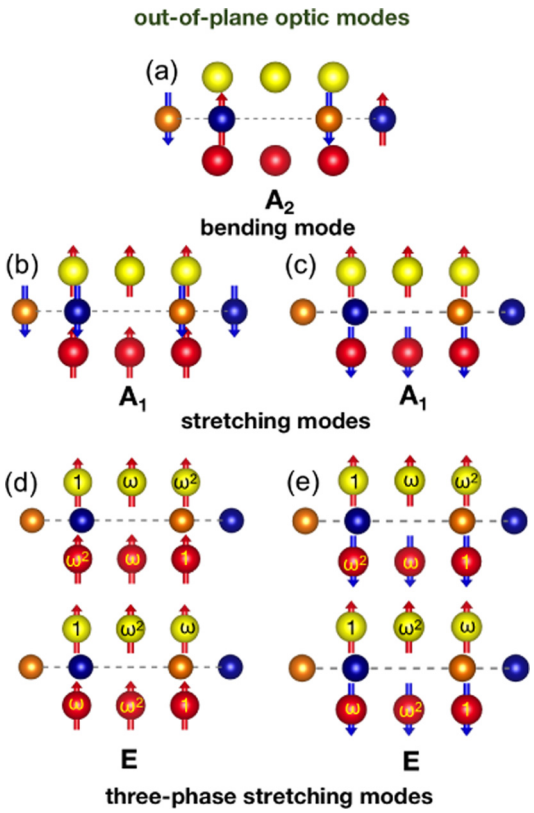

Fig. 2 The eigenvectors of z-axis optic modes in F_3–Cr_2–I_3, where $\omega = e^{i2\pi/3}$, $(1,\omega,\omega^2)$ indicates the relative phases of corresponding atoms; the phases of all unlabeled vibrating atoms default to 1; the arrows represent the direction of the atomic vibration, while their colors have no particular meaning.

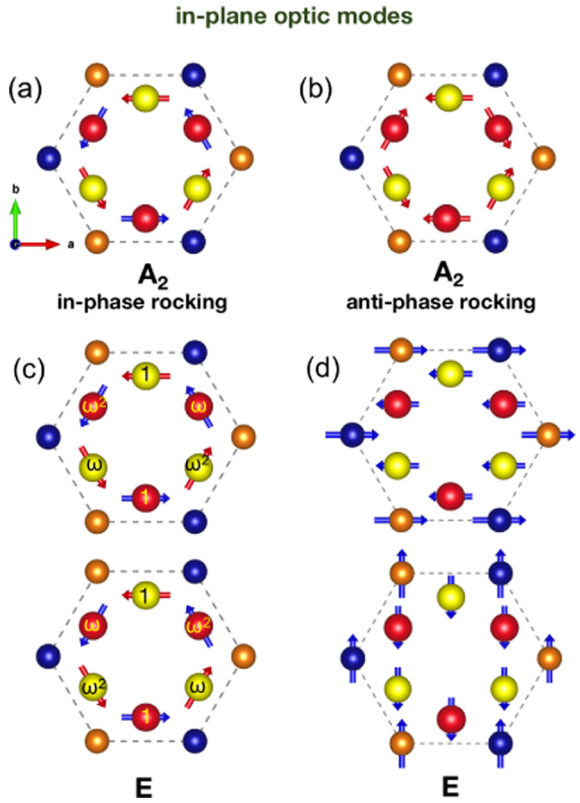

Fig. 3 The eigenvectors of the in-plane optic modes in F_3–Cr_2–I_3, where $\omega = e^{i2\pi/3}$; $(1,\omega,\omega^2)$ indicates the relative phases of corresponding atoms; the phases of all unlabeled vibrating atoms default to 1.

Besides, the circular motion of chromium atoms in Fig. 4(c) is necessary for this E mode to keep the mass center from moving. It is worth pointing out that circular motion is one origin of phonon chirality.

If one only considers the vibration of halogen atoms in the unit cell, each A mode including the motion of three F and three I atoms should have a corresponding doubly degenerate E mode, constituting the three eigenfunctions of the $\hat{C}_3$ rotation operator by the three eigenvalues 1, ω and ω^2. Since $\omega^* = \omega^2$, the two eigenfunctions with eigenvalues ω and ω^2 form a doubly degenerate energy level. However, the anti-phase coupling between the acoustic vibrational modes of Cr and halogen atoms can break this correspondence. For example, the A_1 optic mode shown in Fig. 2(b) and the E mode shown in Fig. 3(d). The in-plane E mode of two Cr atoms shown in Fig. 5(d) are not the eigenfunctions of the $\hat{C}_3$ operator and thus do not have a corresponding A mode (A_1 or A_2). This E mode is the same as the E mode in graphene of two carbon atoms. The A_1 mode should be observed in both Raman and infrared spectra; the A_2 mode is both R and IR inactive and thus cannot be detected in optical spectra. All the E modes are both R and IR active and thus should be observed in optical spectra.

In principle, all modes with the same symmetry would be coupled to a certain degree so that any actual mode should be an admixture of the modes with the same irreducible representation. Symmetry analysis cannot obtain the specific value

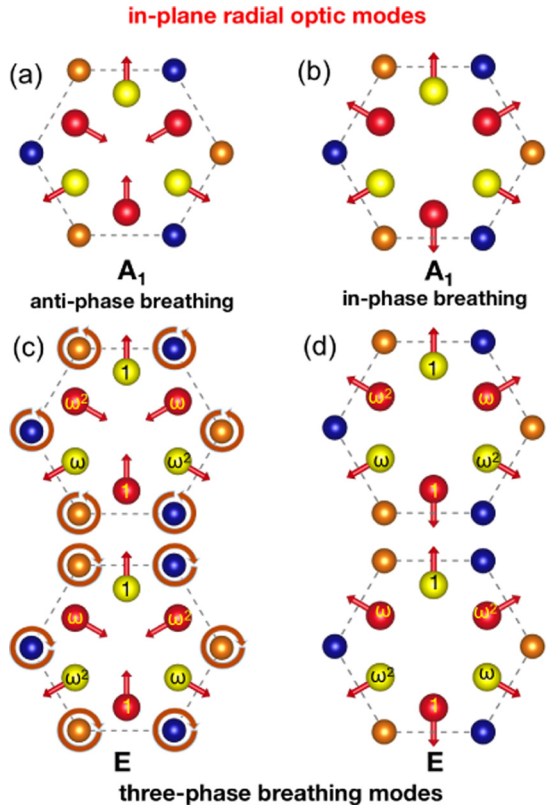

Fig. 4 The eigenvectors of in-plane radial optic modes in F_3–Cr_2–I_3, where $\omega = e^{i2\pi/3}$; $(1,\omega,\omega^2)$ indicates the relative phases of corresponding fluorine and iodine atoms; the relative phases of all unlabeled vibrating atoms default to 1. The circles with an arrow in (c) indicate the circular movements of Cr atoms, which are necessary to keep the mass center of the unit cell still.

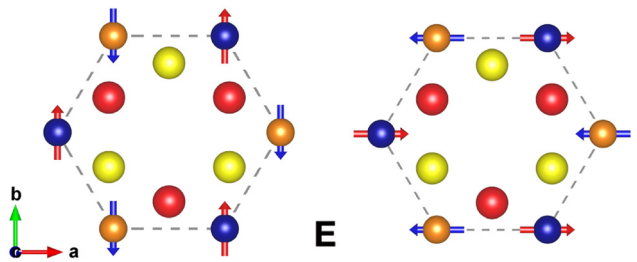

Fig. 5 The eigenvectors for in-plane optic modes of Cr atoms in F_3–Cr_2–I_3.

of vibrational frequency and direction for the mixed mode. Specifically, the in-plane and out-of-plane modes with the same irreducible representation and the same atom must be mixed for the F_3–Cr_2–I_3 monolayer since the F–Cr and I–Cr bonds are neither along purely in-plane directions nor out-of-plane directions. Therefore, the classification based on in-plane and out-of-plane directions is an approximation. On the other hand, considering the significant difference in the mass of F and I atoms as well as in the band strength of F–Cr and I–Cr bonds, the vibrations of F and I atoms thus should be decoupled in some of the practical optical modes of F_3–Cr_2–I_3, which may be distinct from the corresponding optic modes shown in the above figures. Nevertheless, our approximate analysis based on symmetry and direction indeed deepens the understanding of the eigenvectors of the optic modes in Y_3–Cr_2–X_3.

B. Eigenvectors of optic modes in I_3–Cr_2–I_3

Again, for the sake of comparison, we present the vibrational eigenvector of optic phonons in monolayer I_3–Cr_2–I_3, i.e., CrI_3. First, the out-of-plane optic modes are given in Fig. 6. One can see that the A_{2g} mode of Cr atoms of the I_3–Cr_2–I_3 monolayer shown in Fig. 6(a) is the same as the A_2 in F_3–Cr_2–I_3 shown in Fig. 2(a) except for three F atoms substituted by three I atoms. The other two non-degenerate modes A_{2u} and A_{1g} in Fig. 6(b and c) also correspond to the two A_1 modes in Fig. 2(b and c) only by substituting three F atoms. The eigenfunctions of non-degenerate z-axis modes in Fig. 6(a–c) can be written as

$$\begin{aligned} A_{2g}&: \ (z_1 - z_2)_{Cr}, \\ A_{2u}&: \ (z_1 + z_2 + z_3)^{I} + (z_1 + z_2 + z_3)_{I} - (z_1 + z_2)_{Cr}, \\ A_{1g}&: \ (z_1 + z_2 + z_3)^{I} - (z_1 + z_2 + z_3)_{I}, \end{aligned} \tag{21}$$

where the number subscripts represent different atoms; the element superscript and subscript denote iodine atoms on the

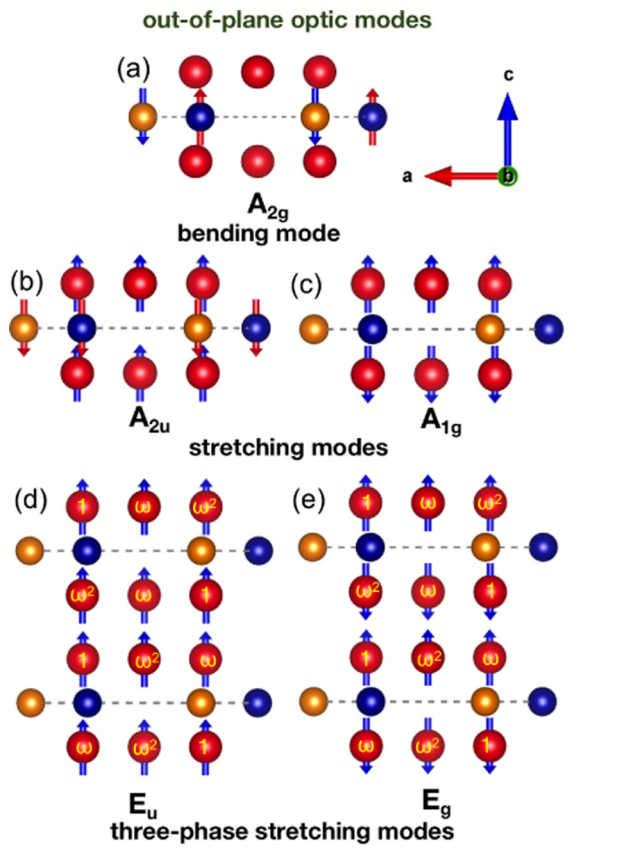

Fig. 6 The eigenvectors of z-axis optic modes in I_3–Cr_2–I_3. Here $\omega = e^{i2\pi/3}$, $(1,\omega,\omega^2)$ indicates the relative phases of corresponding atoms; the phase of all unlabeled vibrating atoms defaults to 1.

top and bottom layers of I_3–Cr_2–I_3, as well as chromium in the middle layer. The corresponding two eigenfunctions for A_1 out-of-plane modes of F_3–Cr_2–I_3 shown in Fig. 2(b and c) are simply

$$\begin{aligned} &A_1(1): \quad (z_1+z_2+z_3)^{F}+(z_1+z_2+z_3)_{I}-(z_1+z_2)_{Cr}, \\ &A_1(2): \quad (z_1+z_2+z_3)^{F}-(z_1+z_2+z_3)_{I}, \end{aligned} \tag{22}$$

just with the I atoms on the top layer substituted by the F atoms. The E_u and E_g are simply with the same correspondence. If we write the eigenfunctions of E_u and E_g modes shown in Fig. 6(d and e) as

$$\begin{aligned} &E_u: \quad \{(z_1+\omega z_2+\omega^2 z_3)^{I}+(z_1+\omega z_2+\omega^2 z_3)_{I}, c.c.\}, \\ &E_g: \quad \{(z_1+\omega z_2+\omega^2 z_3)^{I}-(z_1+\omega z_2+\omega^2 z_3)_{I}, c.c.\}, \end{aligned} \tag{23}$$

here c.c. means complex conjugate, then the eigenfunctions of two out-of-plane E modes in Fig. 2(d and e) should be written as

$$\begin{aligned} &E(1): \quad \{(z_1+\omega z_2+\omega^2 z_3)^{F}+(z_1+\omega z_2+\omega^2 z_3)_{I}, c.c.\}, \\ &E(2): \quad \{(z_1+\omega z_2+\omega^2 z_3)^{F}-(z_1+\omega z_2+\omega^2 z_3)_{I}, c.c.\}. \end{aligned} \tag{24}$$

This correspondence is also applicable for the in-plane radial (r) three-phase breathing modes except for the circular motion of Cr atoms to limit the translational motion of the center of unit cell mass. For the in-plane radial (r) optic modes in Fig. 8(a–d), their eigenfunctions are

$$\begin{aligned} &A_{2u}: \quad (r_1+r_2+r_3)^{I}-(r_1+r_2+r_3)_{I} \\ &E_u: \quad \{(r_1+\omega r_2+\omega^2 r_3)^{I}-(r_1+\omega r_2+\omega^2 r_3)_{I} \\ &\quad +(r_1^{-}+r_2^{-})_{Cr}, c.c.\}, (r^{\pm}=x\pm iy), \\ &A_{1g}: \quad (r_1+r_2+r_3)^{I}+(r_1+r_2+r_3)_{I}, \\ &E_g: \quad \{(r_1+\omega r_2+\omega^2 r_3)^{I}+(r_1+\omega r_2+\omega^2 r_3)_{I}, c.c.\}. \end{aligned} \tag{25}$$

Substituting the I on superscripts by F in the above eigenfunctions, one would get the eigenfunctions for optic modes shown in Fig. 4(a–d):

$$\begin{aligned} &A_1: \quad (r_1+r_2+r_3)^{F}-(r_1+r_2+r_3)_{I} \\ &E: \quad \{(r_1+\omega r_2+\omega^2 r_3)^{F}-(r_1+\omega r_2+\omega^2 r_3)_{I} \\ &\quad +(r_1^{-}+r_2^{-})_{Cr}, c.c.\}, (r^{\pm}=x\pm iy), \\ &A_1: \quad (r_1+r_2+r_3)^{F}+(r_1+r_2+r_3)_{I}, \\ &E: \quad \{(r_1+\omega r_2+\omega^2 r_3)^{F}+(r_1+\omega r_2+\omega^2 r_3)_{I}, c.c.\}. \end{aligned} \tag{26}$$

For the optic modes vibrating along in-plane tangential (t) and rectangular coordinate axes (x, y) directions shown in Fig. 7(a–d),

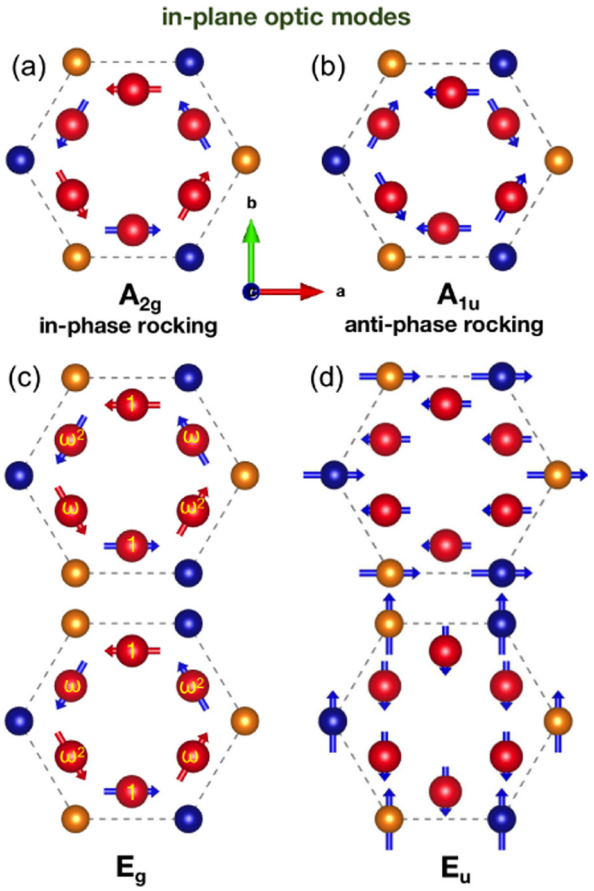

Fig. 7 The eigenvectors of in-plane optic modes of F and I atoms in I_3–Cr_2–I_3. Here $\omega = e^{i2\pi/3}$, $(1,\omega,\omega^2)$ indicates the relative phases of the corresponding atoms; the phase of all unlabeled vibrating atoms defaults to 1.

theirs eigenfunctions are

$$\begin{aligned} &A_{2g}: \quad (t_1+t_2+t_3)^{I}+(t_1+t_2+t_3)_{I}, \\ &E_g: \quad \{(t_1+\omega t_2+\omega^2 t_3)^{I}+(t_1+\omega t_2+\omega^2 t_3)_{I}, c.c.\}, \\ &A_{1u}: \quad (t_1+t_2+t_3)^{I}-(t_1+t_2+t_3)_{I}, \\ &E_u^{x}: \quad \{(x_1+x_2)_{Cr}-(x_1+x_2+x_3)^{I}-(x_1+x_2+x_3)_{I}\}, \\ &E_u^{y}: \quad \{(y_1+y_2)_{Cr}-(y_1+y_2+y_3)^{I}-(y_1+y_2+y_3)_{I}\}. \end{aligned} \tag{27}$$

The linear combinations $E_u^x \pm iE_u^y$ become the eigenfunctions of the $\hat{C}_3$ operator with eigenvalues ω^* and ω, which represent the chiral phonons with pseudo angular momentum 1.

Indeed, the in-plane optic modes of Cr atoms would mix with that of halogen atoms with the same irreducible representation to some extent. Fig. 9 shows the E_g optic mode. It can be seen that the distance between Cr atoms varying during vibration is particularly sensitive to the magnetic order of CrI_3.[15] Webster *et al.* found that when the magnetic order transitions from anti-ferromagnetic (AFM) to FM, the frequency of E_g modes increases while their intensity decreases, which corresponds to distinct spin–phonon interaction.[15] The frequency increase is due to the enhancement of the effective

force constant by super-exchange interaction in the ferromagnetic phase. This spin–phonon interaction is also present at the transition of interlayer magnetic order which has been reported in a magneto-Raman spectroscopy study of multilayered CrI_3.[9]

V. Discussions

A. Magnetic-phonon coupling effect of IR active phonons

The IR active optic phonons could couple with photons directly and thus can be detected by infrared absorption spectrometry. For the X_3–Cr_2–X_3 (such as CrI_3) monolayer, there are five IR active phonons including two non-degenerate A_{2u} modes and three double-degenerate E_u modes. As discussed in the above section, they are Raman inactive modes and thus cannot be detected by Raman spectrometry. One of the two A_{2u} phonons is an out-of-plane stretching mode including both Cr and I atom vibration, as shown in Fig. 6(b); the other A_{2u} phonon is an in-plane anti-phase breathing mode shown in Fig. 8(a). They should be detected by IR optical spectrometry and would change their frequencies with magnetic order variation since

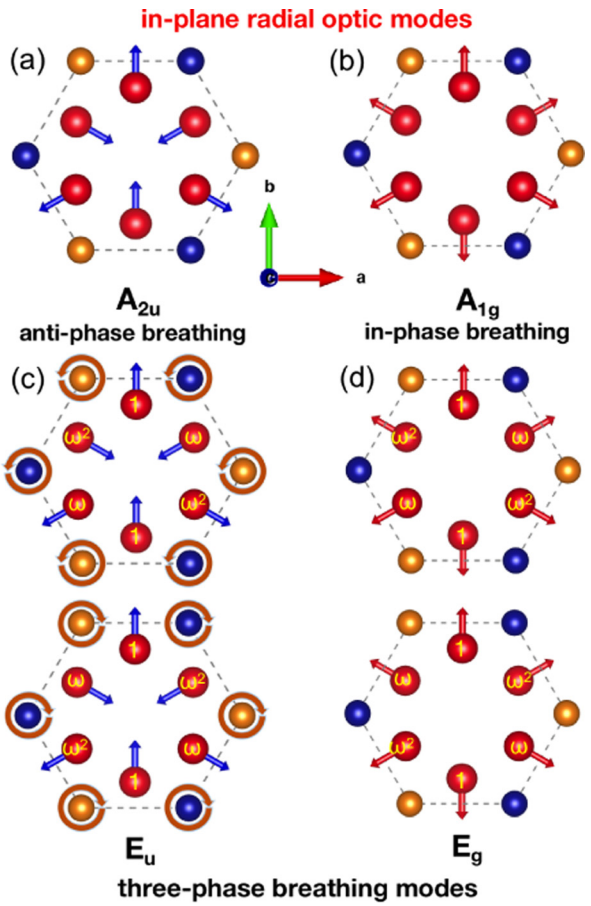

Fig. 8 The eigenvectors of the in-plane radial optic modes of F and I atoms in I_3–Cr_2–I_3. Here $\omega = e^{i2\pi/3}$, $1,\omega,\omega^2$ indicate the relative phases of the corresponding atoms; the phase of all unlabeled vibrating atoms defaults to 1. The circles with an arrow in (c) indicate the circular movements of Cr atoms, which are necessary to keep the mass center of the unit cell still.

Wang *et al.* have found that the frequencies of the two IR modes are significantly influenced by the magnetic configuration.[13] The double-degenerate E_u phonons shown in Fig. 6(d) are three-phase stretching modes only containing motions of non-magnetic I atoms and cannot couple to the magnetic order, whereas the other two E_u modes shown in Fig. 8(c) and 7(d) are breathing and rocking modes respectively, which all include the motion of magnetic Cr atoms and thus can directly couple to the magnetic order of the X_3–Cr_2–X_3 monolayer. Our conclusions are consistent with the experimental infrared spectra of the CrI_3 monolayer, where all five IR modes have been observed.[17]

In stark contrast, for the Janus Y_3–Cr_2–X_3 (such as F_3–Cr_2–I_3) monolayer, all IR active modes obtain the R activity. In particular, the out-of-plane stretching mode including Cr atoms transforms from an IR active A_{2u} mode of the CrI_3 monolayer shown in Fig. 6(b) to an IR and R double-active A_1 mode of the F_3–Cr_2–I_3 monolayer shown in Fig. 2(b). Its frequency is higher than that of the corresponding A_{2u} mode in CrI_3 and lower than that in the CrF_3 monolayer. Therefore, this out-of-plane stretching A_1 mode can behave as a characteristic peak in the optical spectra of the Janus Y_3–Cr_2–X_3 monolayer. Additionally, its frequency variation with magnetic order may also be detected by comparison of the Raman spectra of the FM and AFM Y_3–Cr_2–X_3 monolayer. Contrastively, the E_u mode in Fig. 6(d) transforms to the E mode shown in Fig. 2(d) and is both IR and R active too, and owing to the absence of Cr atoms, its frequency is insensitive to the magnetic order of the F_3–Cr_2–I_3 monolayer. The remaining two E modes shown in Fig. 4(c) and 3(d) include the motion of Cr atoms and thus are coupled to the magnetic order, which can be demonstrated by peak splitting in both infrared and Raman spectra of the magnetic Janus Y_3–Cr_2–X_3 monolayer.

B. Magneto-optical effect of R active phonons A_{1g} and A_1

The magneto-optical effect can be observed in a non-magnetic system under an external magnetic field or magnetic (such as FM and AFM) system. In principle, time-reversal symmetry breaking can induce an extra antisymmetric off-diagonal component to the Raman tensor of A_{1g} and A_1 shown in Table 6. It is this antisymmetric component that generated the polarization rotation of the scattered light. The magneto-optical Kerr effect of A_{1g} phonons (as shown in Fig. 6(c)) due to the FM order has been observed in CrI_3.[10] The polarization rotation in this magneto-optical Kerr effect induced by a monolayer FM insulator is extraordinarily large, being two orders of magnitude larger than that from the magneto-optical Raman effect induced by an external magnetic field.[10]

In contrast, the magneto-optical Kerr effect of the A_g mode in the FM $CrBr_3$ monolayer is negligible while the magneto-optical Raman effect is significant and even named the giant magneto-optical Raman effect.[38] This implies that the mechanism of the magneto-optical Kerr effect resulting from the FM order may be sharply different from the magneto-optical Raman effect induced by the external magnetic field and is worthy of in-depth exploration. Consider that the A_1 irreducible representation in C_{3v} has the same Raman tensor as that of A_{1g} in D_{3d}, one can expect to observe the same magneto-optical

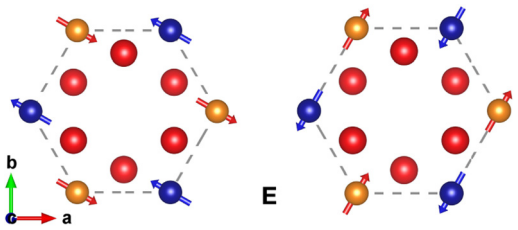

Fig. 9 The eigenvectors for in-plane optic modes of Cr atoms in I_3–Cr_2–I_3.

effect of the corresponding A_1 mode shown in Fig. 2(c). The A_{2u} of the X_3–Cr_2–X_3 monolayer shown in Fig. 6(b), though also with the out-of-plane vibration, is R inactive and thus has no magneto-optical effect. However, for the Janus Y_3–Cr_2–X_3 monolayer without inversion symmetry, it transforms into A_1 shown in Fig. 2(b), which is R active and thus can also exhibit the magneto-optical effect. Furthermore, it is in sharp contrast to the A_1 mode shown in Fig. 2(c), because it contains the vibration of magnetic Cr atoms. Thus one can expect to observe a remarkable magneto-optical effect of this A_1 mode in the Janus Y_3–Cr_2–X_3 monolayer in the FM phase. This reinforces our conclusion in the above subsection that the A_1 mode shown in Fig. 2(b) can behave as a characteristic peak in the optical spectra of the Janus Y_3–Cr_2–X_3 monolayer.

C. Chiral phonons and their effects

In a crystal with C_3 symmetry, chiral phonons at high-symmetry points have pseudo angular momentum ($l_{ph} = 0, \pm 1$) defined by a transform property under a $\hat{C}_3$ rotational operator (rotation by $2\pi/3$ about the z axis): $\hat{C}_3 u(\mathbf{r}) = e^{\left(-i\frac{2\pi}{3}l_{ph}\right)} u(\mathbf{r}) = \omega^{(-l_{ph})} u(\mathbf{r})$.[29] The phonon mode with $l_{ph} = 0$ has 1D irreducible representation, while the corresponding $l_{ph} = \pm 1$ modes have 2D irreducible representation if the inversion symmetry is not broken for the non-magnetic system.

For the X_3–Cr_2–X_3 monolayer, the E_g modes shown in Fig. 6(e), 8(d), and 7(c) are chiral phonons with $l_{ph} = \pm 1$, and chirality can be observed in helicity-resolved Raman scattering. The E_u modes shown in Fig. 6(d) and 8(c) can also be observed directly in infrared absorption optical spectra. In practice, all the E_g modes would mix to some extent, and all the E_u modes would mix too, which may suppress the chirality of the phonon, especially for chiral phonons at the Γ point. Nevertheless, the chiral phonon and its complete switch of the polarization of an incident circularly polarized light involved in a Raman scattering process has been observed in a $CrBr_3$ 2D magnet,[38] which indicates that the incident circularly polarized light may induce or enhance the chirality of doubly degenerate phonons. Therefore we can expect to observe chiral phonons in other 2D X_3–Cr_2–X_3 monolayers.

For the Janus Y_3–Cr_2–X_3 monolayer, all the E modes, such as those shown in Fig. 2(d, e) and 4(c, d), are chiral phonons with pseudo angular momentum $l_{ph} = \pm 1$, whose chirality should also be observed in both helicity-resolved Raman scattering and infrared absorption optical experiments. These chiral phonons are even easier to observe than those in the X_3–Cr_2–X_3 monolayer because of the absence of inversion symmetry.

In addition, the E modes including Cr atoms in Fig. 3(d) and 5, or the E_u mode in Fig. 7(d) as well as the E_g mode in Fig. 9, are in-plane shear modes, of which two partners (u_1, u_2) can be combined into chiral phonons with partners $u_1 \pm iu_2$, which represent the circular motion of Cr atoms. These chiral phonons not only have pseudo angular momentum but also have real angular momentum,[37] while their non-zero real angular momentum is only emergent in the system without time reversal or space inversion symmetry. The orbit magnetic moment of these chiral phonons should be coupled to the spin magnetic moment of the Cr atom in magnetic Y_3–Cr_2–X_3 and X_3–Cr_2–X_3, which would lead to the degeneracy lifting of 2D chiral phonons in the FM phase. Furthermore, for the E_u mode in Fig. 8(c) with inversion symmetry, its vibration includes the circular motion of Cr atoms, thus the angular momentum can only be realized in the magnetic X_3–Cr_2–X_3 monolayer; while for the corresponding E mode in Fig. 4(c), its non-zero angular momentum can also be realized in the non-magnetic Y_3–Cr_2–X_3 monolayer due to the absence of inversion symmetry.

We find that there are two distinct types of chiral phonons at Γ for the Y_3–Cr_2–X_3 monolayer with (X, Y) $\in$ {F, Cl, Br, I}, both of them have 2D irreducible representation, one with only pseudo angular momentum but the other also with real angular momentum. This seems to imply that the chirality of a phonon does not always mean the circular polarization of a phonon, in other words, the circular motion of involving atoms. The chirality would be exhibited in helicity-resolved optical spectra even for a non-magnetic system with spatial inversion symmetry, while the non-zero angular momentum of phonons would lead to spectral splitting of degenerated chiral phonons due to the coupling of its magnetic momentum to the spin of magnetic atoms. Thus we conclude that the chirality of a phonon is determined by its pseudo rather than real angular momentum.

VI. Conclusions

In conclusion, we have performed a group theory investigation on the optical phonons in monolayer X_3–Cr_2–X_3 and their Janus structures Y_3–Cr_2–X_3. The irreducible representation of all phonons at the Γ point and the IR and R activity of optic phonons have been obtained. The Raman tensors, the linear polarization assignments of Raman active phonons, and the compatibility relationship of phonon irreducible representation between Y_3–Cr_2–X_3 and X_3–Cr_2–X_3 monolayer are offered, which provides essential guidance for further optical spectral identification of Janus Y_3–Cr_2–X_3. Furthermore, the corresponding phonon eigenfunctions and their corresponding schematic representations facilitate the experimental identification of their optic phonons. We conclude that: (1) the out-of-plane stretching A_1 mode including both Cr and halogen atoms may be manifested as a characteristic peak in the optical spectra of the Janus Y_3–Cr_2–X_3 monolayer; (2) the giant magneto-optical effect of the corresponding A_1 mode in the FM Janus Y_3–Cr_2–X_3 monolayer

should be observed in the polarized Raman spectra experiment; (3) the chiral phonons at Γ in the Y_3–Cr_2–X_3 monolayer should be revealed in helicity-resolved optical spectra. Our work enriches the detailed understanding of optic phonons in the Y_3–Cr_2–X_3 monolayer with (X, Y) $\in$ {F, Cl, Br, I}, and offers theoretical guidance for exploring their distinct physical effects experimentally.

Author contributions

Y. C. Liu: conceptualization, formal analysis, writing – original draft, visualization, investigation; H. B. Niu: conceptualization, formal analysis, data curation, writing – review and editing, project administration; J. B. Lin: formal analysis, validation, writing – review and editing; V. Wang: data curation, writing – review and editing, visualization, funding acquisition, supervision.

Conflicts of interest

There are no conflicts to declare.

Acknowledgements

This work was supported by the Doctoral Research Start-up Funds of Teachers at Xi'an University of Technology (Grant No. 109-451119001) and partly by the Natural Science Basic Research Program of Shaanxi (Program No. 2022JQ-063). H. B. Niu acknowledges the financial support of the Natural Science Foundation of Shaanxi Province, China (No. 2021JM-541). V. W. acknowledges the Natural Science Basic Research Program of Shaanxi (Program No. 2021JQ-464), The Natural Science Basic Research Plan of Shaanxi Province (Grant No. 2021JZ-48), The Scientific Research Program Funded by Shaanxi Provincial Education Department (Grant No. 21JP088 and 22JP058), and The Youth Innovation Team of Shaanxi Universities and Center for Computational Materials Science, Institute for Materials Research, Tohoku University for the use of MASAMUNE-IMR (Project No. 2112SC0503).

References

1 M. A. McGuire, H. Dixit, V. R. Cooper and B. C. Sales, *Chem. Mater.*, 2015, **27**(2), 612–620.
2 B. Huang, G. Clark, E. Navarro-Moratalla, D. R. Klein, R. Cheng, K. L. Seyler, D. Zhong, E. Schmidgall, M. A. McGuire and D. H. Cobden, *et al.*, *Nature*, 2017, **546**(7657), 270–273.
3 J. L. Lado and J. Fernández-Rossier, *2D Mater.*, 2017, **4**(3), 035002.
4 N. Sivadas, S. Okamoto, X. Xu, C. J. Fennie and D. Xiao, *Nano Lett.*, 2018, **18**(12), 7658–7664.
5 B. Huang, G. Clark, D. R. Klein, D. MacNeill, E. Navarro-Moratalla, K. L. Seyler, N. Wilson, M. A. McGuire, D. H. Cobden and D. Xiao, *et al.*, *Nat. Nanotechnol.*, 2018, **13**(7), 544–548.
6 P. Jiang, L. Li, Z. Liao, Y. Zhao and Z. Zhong, *Nano Lett.*, 2018, **18**(6), 3844–3849.
7 D. Soriano, C. Cardoso and J. Fernández-Rossier, *Solid State Commun.*, 2019, **299**, 113662.
8 S. I. Vishkayi, Z. Torbatian, A. Qaiumzadeh and R. Asgari, *Phys. Rev. Mater.*, 2020, **4**, 094004.
9 A. McCreary, T. T. Mai, F. G. Utermohlen, J. R. Simpson, K. F. Garrity, X. Feng, D. Shcherbakov, Y. Zhu, J. Hu and D. Weber, *et al.*, *Nat. Commun.*, 2020, **11**(1), 3879.
10 B. Huang, J. Cenker, X. Zhang, E. L. Ray, T. Song, T. Taniguchi, K. Watanabe, M. A. McGuire, D. Xiao and X. Xu, *Nat. Nanotechnol.*, 2020, **15**(3), 212–216.
11 K. Yang, W. Hu, H. Wu, M.-H. Whangbo, P. G. Radaelli and A. Stroppa, *ACS Appl. Electron. Mater.*, 2020, **2**(5), 1373–1380.
12 W. Jin, H. H. Kim, Z. Ye, G. Ye, L. Rojas, X. Luo, B. Yang, F. Yin, J. S. A. Horng and S. Tian, *et al.*, *Nat. Commun.*, 2020, **11**(1), 4780.
13 K. Wang, W.-X. Zhou, Y. Cheng, M. Zhang, H. Wang and G. Zhang, *Nanoscale*, 2021, **13**, 10882–10890.
14 D. T. Larson and E. Kaxiras, *Phys. Rev. B*, 2018, **98**, 085406.
15 L. Webster, L. Liang and J.-A. Yan, *Phys. Chem. Chem. Phys.*, 2018, **20**(36), 23546–23555.
16 K. Wang, W. Zhou, Y. Cheng, M. Zhang, H. Wang and G. Zhang, *Nanoscale*, 2021, **13**, 10882–10890.
17 L. Tomarchio, S. Macis, L. Mosesso, L. T. Nguyen, A. Grilli, M. C. Guidi, R. J. Cava and S. Lupi, *Sci. Rep.*, 2021, **11**(1), 23405.
18 A.-Y. Lu, H. Zhu, J. Xiao, C.-P. Chuu, Y. Han, M.-H. Chiu, C.-C. Cheng, C.-W. Yang, K.-H. Wei and Y. Yang, *et al.*, *Nat. Nanotechnol.*, 2017, **12**(8), 744–749.
19 L. Dong, J. Lou and V. B. Shenoy, *ACS Nano*, 2017, **11**(8), 8242–8248.
20 M. Yagmurcukardes, C. Sevik and F. M. Peeters, *Phys. Rev. B*, 2019, **100**, 045415.
21 Y. Chen, J. Liu, J. Yu, Y. Guo and Q. Sun, *Phys. Chem. Chem. Phys.*, 2019, **21**(3), 1207–1216.
22 A. Rawat, M. K. Mohanta, N. Jena, Dimple, R. Ahammed and A. De Sarkar, *J. Phys. Chem. C*, 2020, **124**(19), 10385–10397.
23 X. Li, Y. Ge, J. Li, W. Wan and Y. Liu, *Chin. Phys. B*, 2021, **30**(10), 107305.
24 N. Sun, X. Wang and W. Mi, *Phys. Chem. Chem. Phys.*, 2021, **23**, 17338–17347.
25 F. Zhang, W. Mi and X. Wang, *Adv. Electron. Mater.*, 2020, **6**(1), 1900778.
26 F. Zhang, H. Zhang, W. Mi and X. Wang, *Phys. Chem. Chem. Phys.*, 2020, **22**(16), 8647–8657.
27 R. Albaridy, A. Manchon and U. Schwingenschlögl, *J Phys: Condens. Matter*, 2020, **32**(35), 355702.
28 H. Niu, Y. Liu, J. Shi and V. Wang, *Materials*, 2022, **15**(13), 4418.
29 L. Zhang and Q. Niu, *Phys. Rev. Lett.*, 2015, **115**, 115502.
30 H. Zhu, J. Yi, M.-Y. Li, J. Xiao, L. Zhang, C.-W. Yang, R. A. Kaindl, L.-J. Li, Y. Wang and X. Zhang, *Science*, 2018, **359**(6375), 579–582.
31 H. Chen, W. Zhang, Q. Niu and L. Zhang, *2D Mater.*, 2018, **6**(1), 012002.
32 X. Chen, X. Lu, S. Dubey, Q. Yao, S. Liu, X. Wang, Q. Xiong, L. Zhang and A. Srivastava, *Nat. Phys.*, 2019, **15**(3), 221–227.
33 H. Chen, W. Wu, S. A. Yang, X. Li and L. Zhang, *Phys. Rev. B*, 2019, **100**, 094303.

34 E. Liu, J. van Baren, T. Taniguchi, K. Watanabe, Y.-C. Chang and C. H. Lui, *Phys. Rev. Res.*, 2019, **1**, 032007.
35 N. Suri, C. Wang, Y. Zhang and D. Xiao, *Nano Lett.*, 2021, **21**(23), 10026–10031.
36 Q. Wang, S. Li, J. Zhu, H. Chen, W. Wu, W. Gao, L. Zhang and S. A. Yang, *Phys. Rev. B*, 2022, **105**, 104301.
37 T. Zhang and S. Murakami, *Phys. Rev. Res.*, 2022, **4**, L012024.
38 T. Yin, K. A. Ulman, S. Liu, A. Granados del Águila, Y. Huang, L. Zhang, M. Serra, D. Sedmidubsky, Z. Sofer, S. Y. Quek and Q. Xiong, *Adv. Mater.*, 2021, **33**(36), 2101618.
39 L. M. Malard, M. H. D. Guimarães, D. L. Mafra, M. S. C. Mazzoni and A. Jorio, *Phys. Rev. B: Condens. Matter Mater. Phys.*, 2009, **79**, 125426.
40 J. Ribeiro-Soares, R. M. Almeida, L. G. Cançado, M. S. Dresselhaus and A. Jorio, *Phys. Rev. B: Condens. Matter Mater. Phys.*, 2015, **91**, 205421.
41 X. Lu, X. Luo, J. Zhang, S. Y. Quek and Q. Xiong, *Nano Res.*, 2016, **9**(12), 3559–3597.
42 M. S. Dresselhaus, G. Dresselhaus and A. Jorio, *Group theory: application to the physics of condensed matter*, Springer Science & Business Media, 2010.
43 Y. C. Liu, V. Wang, M. G. Xia and S. L. Zhang, *J. Phys.: Condens. Matter*, 2017, **29**(9), 095702.
44 S. Djurdjić Mijin, A. Šolajić, J. Pešić, M. Šćepanović, Y. Liu, A. Baum, C. Petrovic, N. Lazarević and Z. V. Popović, *Phys. Rev. B*, 2018, **98**, 104307.
45 Y. C. Liu, H. B. Niu and J. B. Lin, *Phys. Chem. Chem. Phys.*, 2022, **24**, 17895–17897.
46 L. Webster, L. Liang and J.-A. Yan, *Phys. Chem. Chem. Phys.*, 2022, **24**, 17898.
47 H. Wang, V. Eyert and U. Schwingenschlögl, *J. Phys.: Condens. Matter*, 2011, **23**(11), 116003.

